

DC-VSR: Spatially and Temporally Consistent Video Super-Resolution with Video Diffusion Prior

JANGHYEOK HAN*, POSTECH, Republic of Korea

GYUJIN SIM*, POSTECH, Republic of Korea

GEONUNG KIM, POSTECH, Republic of Korea

HYUN-SEUNG LEE, Visual Display Business, Samsung Electronics, Republic of Korea

KYUHA CHOI, Visual Display Business, Samsung Electronics, Republic of Korea

YOUNGSEOK HAN, Visual Display Business, Samsung Electronics, Republic of Korea

SUNGHYUN CHO, POSTECH, Republic of Korea

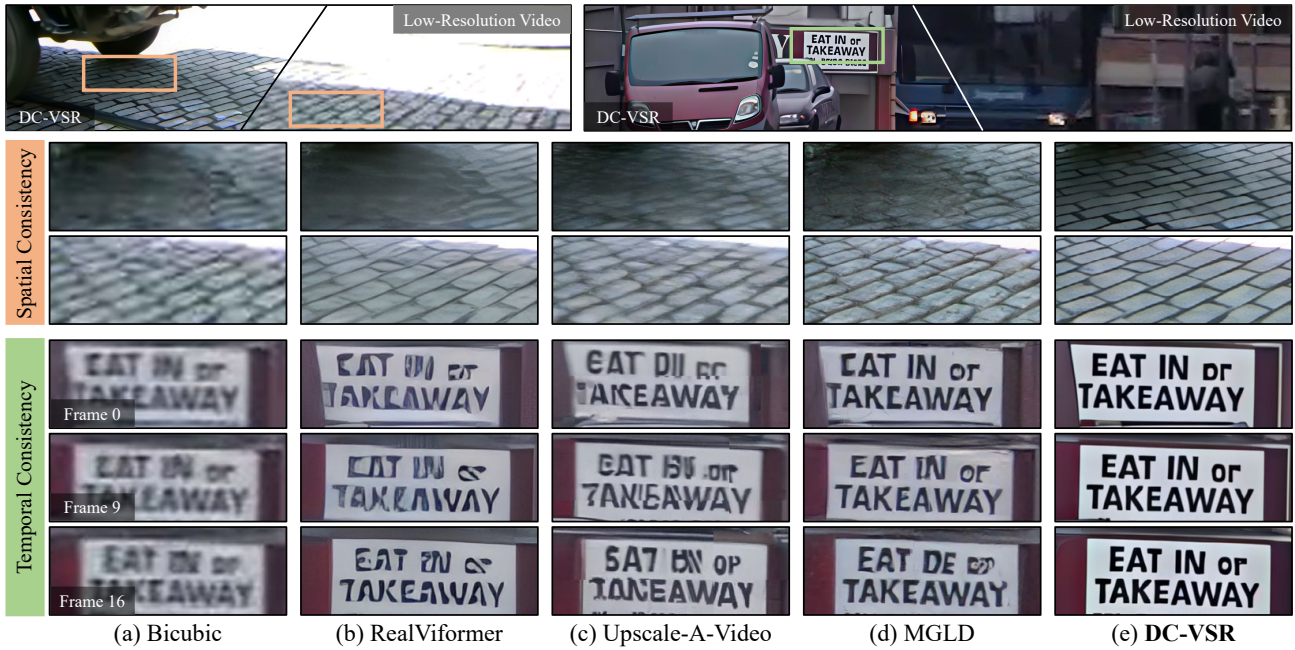


Fig. 1. Real-world video super-resolution results of our proposed methods and state-of-the-art models: RealViformer [Zhang and Yao 2024], Upscale-A-Video [Zhou et al. 2024], MGLD [Yang et al. 2024a]. DC-VSR shows outstanding super-resolution performance, in respect of not only quality but also spatial and temporal consistency. The input videos are from the VideoLQ dataset [Chan et al. 2022b] (samples 037 and 038).

Video super-resolution (VSR) aims to reconstruct a high-resolution (HR) video from a low-resolution (LR) counterpart. Achieving successful VSR requires producing realistic HR details and ensuring both spatial and temporal consistency. To restore realistic details, diffusion-based VSR approaches have recently been proposed. However, the inherent randomness of diffusion, combined with their tile-based approach, often leads to spatio-temporal inconsistencies. In this paper, we propose DC-VSR, a novel VSR approach to produce spatially and temporally consistent VSR results with realistic textures. To achieve spatial and temporal consistency, DC-VSR adopts a novel

Spatial Attention Propagation (SAP) scheme and a Temporal Attention Propagation (TAP) scheme that propagate information across spatio-temporal tiles based on the self-attention mechanism. To enhance high-frequency details, we also introduce Detail-Suppression Self-Attention Guidance (DSSAG), a novel diffusion guidance scheme. Comprehensive experiments demonstrate that DC-VSR achieves spatially and temporally consistent, high-quality VSR results, outperforming previous approaches. The project page is available at <https://daramgc.github.io/docs/Publications/dc-vsr>

CCS Concepts: • **Computing methodologies** → **Computational photography**.

Additional Key Words and Phrases: Video Super-Resolution, Real-World Video, Video Generative Prior

1 INTRODUCTION

Video super-resolution (VSR) is a task to restore a high-resolution (HR) video from a low-resolution (LR) counterpart, which has a vast array of applications, such as enhancing old footage and improving

*Both authors contributed equally to this research.

Authors' addresses: Janghyeok Han, POSTECH, Republic of Korea, hjh9902@postech.ac.kr; Gyu Jin Sim, POSTECH, Republic of Korea, sgj0402@postech.ac.kr; Geonung Kim, POSTECH, Republic of Korea, k2woong92@postech.ac.kr; Hyun-Seung Lee, Visual Display Business, Samsung Electronics, Republic of Korea, hyuns.lee@samsung.com; Kyuha Choi, Visual Display Business, Samsung Electronics, Republic of Korea, kyuha75.choi@samsung.com; Youngseok Han, Visual Display Business, Samsung Electronics, Republic of Korea, yseok.han@samsung.com; Sunghyun Cho, POSTECH, Republic of Korea, s.cho@postech.ac.kr.

streaming video quality on limited bandwidths. However, VSR is particularly challenging due to its severely ill-posed nature of the problem, primarily because of the missing high-frequency information in LR videos caused during the sampling process. Furthermore, real-world videos face a myriad of unknown degradation factors beyond just sampling issues, including noise, compression artifacts, and various other distortions, making the task even more ill-posed.

To achieve successful VSR, it is essential to generate realistic HR details while maintaining both spatial and temporal consistency. To this end, over the past few decades, numerous approaches have been proposed, including traditional methods such as interpolation techniques, model-based optimization approaches, and recent neural network-based ones [Zhang and Yao 2024]. Nevertheless, most of them struggle to produce realistic HR details due to a lack of effective priors that model high-frequency details as shown in Fig. 1(b).

Recently, diffusion models that provide powerful generative priors for natural images have been exploited for VSR to achieve high-quality results with realistic textures. Yang *et al.* [2024a] and Zhou *et al.* [2024] utilize image diffusion models and successfully restore detail-rich HR videos. However, adopting image diffusion models poses challenges in maintaining spatial and temporal consistency due to the design of image diffusion models, which typically target single images with limited spatial sizes due to significant memory usage. To achieve temporally-consistent VSR using image diffusion models, these approaches adopt additional temporal layers, temporal propagation with motion compensation, and overlapping of temporal windows. Furthermore, to handle large video frames, frames are split into overlapping tiles, processed individually, and then merged. Despite these efforts, resulting videos often suffer from spatial and temporal inconsistencies due to the inherent randomness of image diffusion models and their tile-based approach (Fig. 1(c) and (d)).

In this paper, we propose *DC-VSR (Diffusion-based Consistent VSR)*, a novel VSR approach that, for the first time, leverages a video diffusion prior. Our approach produces spatially and temporally consistent results with realistic textures, given an LR video of arbitrary length and spatial size (Fig. 1(e)). We employ Stable Video Diffusion (SVD) [StabilityAI 2023] as a video diffusion prior, which provides powerful generative capabilities for restoring high-quality, temporally-consistent details. However, exploiting an existing video diffusion model for consistent VSR over long video clips with large frames is challenging, as existing models are designed to synthesize a limited number of small frames, similar to image diffusion models.

To achieve spatial and temporal consistency for a long video with large frames, DC-VSR introduces a novel Spatial Attention Propagation (SAP) scheme and Temporal Attention Propagation (TAP) scheme. Specifically, DC-VSR decomposes an input LR video into multiple spatio-temporal tiles, and processes them separately. To achieve spatial consistency across tiles, SAP introduces a subsampled feature map representing the entire area of a video frame and uses it to process tiles at different spatial locations. On the other hand, TAP enhances temporal consistency across tiles by propagating information between temporally consecutive tiles. Both schemes are realized by extending the self-attention layers of a video diffusion model, enabling information on HR details to be effectively propagated across tiles without losing the generative capability of a pretrained diffusion model.

Additionally, we propose Detail-Suppression Self-Attention Guidance (DSSAG), a novel diffusion guidance scheme to improve high-frequency details in synthesized HR video frames. Similar to Self-Attention Guidance (SAG) [Hong *et al.* 2023] and Perturbed Attention Guidance (PAG) [Ahn *et al.* 2024], DSSAG guides the diffusion process by amplifying high-frequency details in the latent representation. However, unlike the previous methods, DSSAG provides more flexible control over the guidance scale, and can seamlessly integrate with classifier-free guidance (CFG) for high-quality synthesis without incurring additional computational overhead.

We demonstrate the effectiveness of our approach on real-world VSR tasks, where input LR videos contain various unknown degradations. Our experimental results show that DC-VSR achieves spatially and temporally consistent, high-quality VSR results, outperforming previous approaches. Our contributions are summarized as follows:

- We introduce DC-VSR, a novel VSR approach based on a video diffusion prior, which produces spatially and temporally consistent results with realistic textures. Our approach is the first to exploit a video diffusion prior in VSR.
- We propose SAP that injects subsampled features representing the entire area of a video frame to different tiles, ensuring spatial consistency.
- We propose TAP for sharing information across temporally distant frames, achieving temporal consistency.
- We introduce DSSAG to enhance the quality of synthesized video frames without additional computational overhead.

2 RELATED WORK

Generative Prior for Video Super-Resolution. VSR methods can broadly be classified into two main categories based on the use of generative prior. VSR models without generative prior [Chan *et al.* 2021, 2022a,b; Xie *et al.* 2023; Youk *et al.* 2024; Zhang and Yao 2024] are typically trained using reconstruction losses, such as the mean squared error (MSE), augmented with additional techniques designed to enhance temporal consistency. Although they restore HR videos closely matching the input LR videos, they fail to generate complex details, producing blurry results due to the significant ill-posed nature of the problem. To achieve VSR with rich details, generative prior-based VSR methods [Chen *et al.* 2024; Rota *et al.* 2024; Xu *et al.* 2024; Yang *et al.* 2024a; Zhou *et al.* 2024] have recently emerged. These methods fine-tune GANs [Goodfellow *et al.* 2014] or diffusion-based image generation models by modifying them to take LR inputs as conditions and incorporating additional modules to consider temporal consistency. However, maintaining consistency across frames with detailed textures is still challenging [Blattmann *et al.* 2023a,b], leading to temporal flickering artifacts.

Image Super-Resolution. As deep learning techniques have advanced, various image super-resolution (ISR) methods have been proposed. SRCNN [Dong *et al.* 2015] was the first to introduce a CNN-based SR method. Subsequent studies have applied various network architectures, such as residual networks [Kim *et al.* 2016a; Ledig *et al.* 2017], dense networks [Wang *et al.* 2021, 2018b; Zhang *et al.* 2018c], Laplacian pyramid networks [Lai *et al.* 2017], back-projection networks [Haris *et al.* 2018], recursive structures [Kim *et al.* 2016b; Tai *et al.* 2017], and channel attention [Zhang *et al.*

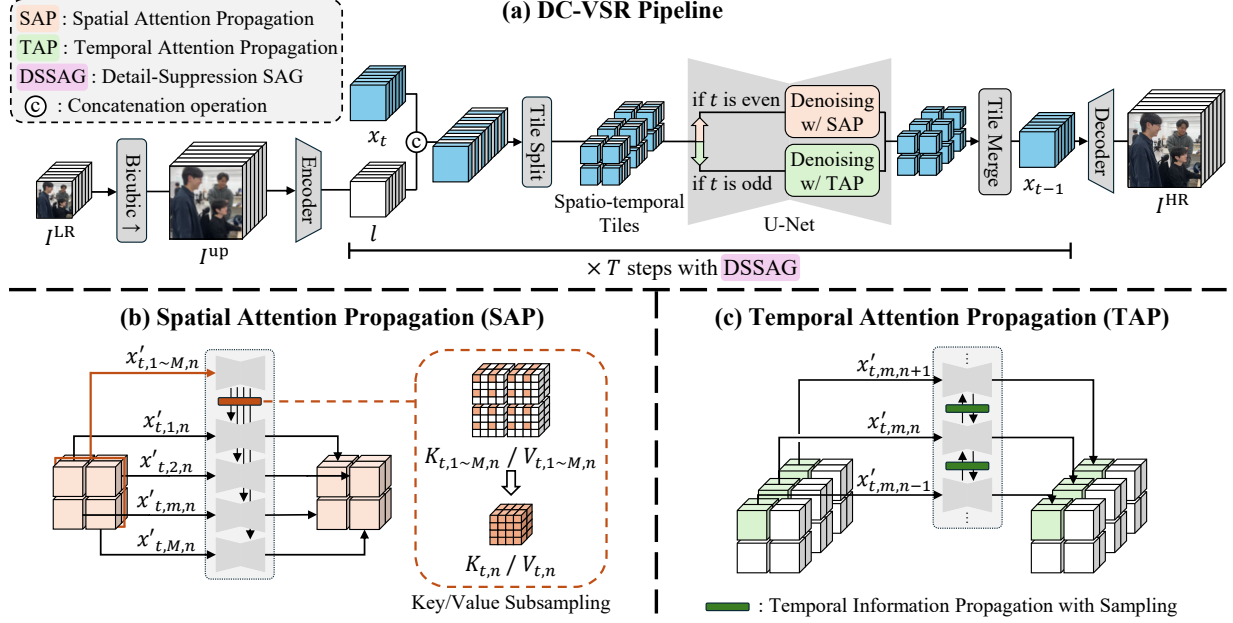


Fig. 2. Overall pipeline of proposed DC-VSR. An encoded low-resolution video latent is concatenated to the current noisy latent x_t , and it undergoes alternating denoising processes using both Spatial Attention Propagation (SAP) and Temporal Attention Propagation (TAP). At this stage, the noisy latent is split and merged before and after the denoising process, respectively. After each denoising step, Detail-Suppression Self-Attention Guidance (DSSAG) is applied to enhance the quality of the image further.

2018b]. While these methods have demonstrated promising SR results, they often struggle to recover high-frequency details. To address this, approaches leveraging the generative prior of pretrained generative models have been introduced exploiting GANs [Chan et al. 2020; Menon et al. 2020] or Diffusion models [Lin et al. 2024; Sun et al. 2024; Wang et al. 2024; Wu et al. 2024a,b; Yang et al. 2024b; Yu et al. 2024]. Since the application of these methods to videos leads to severe flickering artifacts due to the absence of temporal consistency, VSR research has been active in addressing this issue.

Tile-based Generation. Diffusion models face two main challenges in generating higher spatial or temporal resolutions: quality degradation from discrepancies between training and inference conditions, and substantial computational costs. To address these challenges, tile-based generation approaches have been proposed [Bar-Tal et al. 2023; Du et al. 2024; Lee et al. 2023; Yang et al. 2024a; Zhou et al. 2024]. These methods divide the input into overlapping tiles, perform diffusion sampling on each tile individually, and subsequently merge the tiles. However, their approaches do not consider inter-tile consistency, often generating inconsistent details for the same content across split tiles in an image or distant frames [Yang et al. 2024a; Zhou et al. 2024].

3 DC-VSR

Given an input LR video I^{LR} consisting of N frames $\{I_1^{LR}, \dots, I_N^{LR}\}$, DC-VSR produces an HR video I^{HR} . Fig. 2 illustrates the overall framework of DC-VSR, which is built upon the SVD framework [StabilityAI 2023]. To begin, DC-VSR upsamples I^{LR} using bicubic interpolation to match the target resolution, and obtains an upscaled video I^{up} . It then embeds I^{up} into the latent space using the VAE

encoder [Rombach et al. 2022], obtaining a latent representation l , which consists of $[l_1, \dots, l_N]$ stacked along the channel dimension where l_i represents the latent of the i -th upsampled video frame I_i^{up} . To generate an HR video, DC-VSR initializes the latent representation x_T of I^{HR} as random noise, where T is the number of diffusion sampling steps, and x_T is a tensor with the same size as l .

At each diffusion sampling step t , x_t and l are first concatenated in an interleaved manner, i.e., $[x_{t,1}, l_1, \dots, x_{t,N}, l_N]$, where $x_{t,i}$ is the noisy latent of the i -th HR video frame. The concatenated latents are then split into spatio-temporal tiles. We refer to each tile as $x'_{t,m,n}$ where m and n are spatial and temporal indices. Each tile is processed through a denoising U-Net, and the processed tiles are merged to obtain the latent representation x_{t-1} at the next sampling step $t-1$. We utilize spatio-temporal tiles of size $64 \times 64 \times 14$ in the latent space, corresponding to $512 \times 512 \times 14$ in the image space with a scaling factor of 8. In line with previous approaches [Yang et al. 2024a; Zhou et al. 2024], spatially and temporally neighboring tiles overlap by 50%. Overlapped tiles are blended in the tile merging step in our pipeline using alpha blending with Gaussian weights. To achieve spatial and temporal consistency, DC-VSR alternately applies either SAP or TAP at each sampling step until t reaches 0. Finally, x_0 is fed to a decoder, producing the HR video I^{HR} .

DC-VSR employs a tile-based approach to handle lengthy videos with large frames with a video diffusion prior. However, naively splitting a video into tiles may introduce spatial and temporal inconsistencies. In image diffusion models like latent diffusion model (LDM) [Rombach et al. 2022], self-attention layers of the denoising U-Nets ensure spatial consistency within an image. Likewise, video diffusion models such as SVD [StabilityAI 2023] leverage

self-attention to achieve spatially and temporally coherent results. Specifically, the self-attention operation is defined as:

$$\text{SA}(\mathbf{Q}, \mathbf{K}, \mathbf{V}) = \text{softmax}\left(\frac{\mathbf{Q}\mathbf{K}^\top}{\sqrt{d}}\right)\mathbf{V}, \quad (1)$$

where \mathbf{Q} , \mathbf{K} and \mathbf{V} are query, key, and value in the matrix representations, respectively, and d is the attention feature dimension. For a certain spatial and temporal position in a video, the self-attention operation calculates the correlation between the query at position and keys at other positions, and aggregates values based on these correlations. As a result, the synthesized content of any region within the video is harmonized with the rest of the video. However, when a video is split into tiles, each tile undergoes an independent attention process, resulting in spatial and temporal inconsistencies. To address this, DC-VSR extends the self-attention operations using SAP and TAP, allowing attentions to be efficiently computed across tiles. In Sections 3.1 and 3.2, we describe SAP and TAP to achieve spatial and temporal consistency across tiles. We then explain DSSAG to further enhance VSR quality in Section 3.3.

3.1 Spatial Attention Propagation

To achieve spatial consistency across tiles, SAP extends self-attention operations for each tile to incorporate information from different tiles. However, due to the quadratic computational complexity of attention, naïve extension of self-attention operations is practically infeasible. Instead, to avoid the quadratic increase of the computational complexity, SAP leverages subsampled features that represent the entire areas of video frames and injects them into the self-attention operations for each tile.

Fig. 2(b) illustrates the SAP scheme. At diffusion sampling step t for SAP, we feed each tile $x'_{t,m,n}$ to the denoising U-Net. Then, at each self-attention layer, we compute key/value pairs, and subsample them in a spatially uniform manner with respect to a predefined sampling rate s_{SAP} . Finally, we aggregate the subsampled key/value pairs for all $m \in \{1, \dots, M\}$, obtaining the subsampled sets of keys and values, $K_{t,n}$ and $V_{t,n}$. Once $K_{t,n}$ and $V_{t,n}$ are obtained, we inject them into the self-attention operation of each tile. Specifically, let us denote the query, key, and value sets computed from tile $x'_{t,m,n}$ as $Q_{t,m,n}$, $K_{t,m,n}$, and $V_{t,m,n}$, respectively. We construct new sets of keys and values $\hat{K}_{t,m,n}$ and $\hat{V}_{t,m,n}$ by merging $K_{t,m,n}$ and $K_{t,n}$, and $V_{t,m,n}$ and $V_{t,n}$, respectively. Finally, we perform the self-attention operation using the extended keys and values, i.e.,

$$\text{SA}(\mathbf{Q}_{t,m,n}, \hat{\mathbf{K}}_{t,m,n}, \hat{\mathbf{V}}_{t,m,n}) = \text{softmax}\left(\frac{\mathbf{Q}_{t,m,n}\hat{\mathbf{K}}_{t,m,n}^\top}{\sqrt{d}}\right)\hat{\mathbf{V}}_{t,m,n}, \quad (2)$$

where $\mathbf{Q}_{t,m,n}$, $\hat{\mathbf{K}}_{t,m,n}$, and $\hat{\mathbf{V}}_{t,m,n}$ are matrix representations of $Q_{t,m,n}$, $\hat{K}_{t,m,n}$ and $\hat{V}_{t,m,n}$, respectively. We apply the SAP scheme specifically to the first two and last two spatial self-attention layers, as these layers play a crucial role in capturing and synthesizing HR details.

3.2 Temporal Attention Propagation

Fig. 2(c) illustrates the TAP scheme for cross-tile temporal consistency. TAP bidirectionally propagates information from a tile to its neighbor. Specifically, at each diffusion sampling step for TAP, the propagation is performed in either the forward or backward

direction. Without loss of generality, we describe the TAP scheme in the forward direction in the following.

At diffusion sampling step t , we process each tile $x'_{t,m,n-1}$ using the denoising U-Net, and extract keys and values from the self-attention layers. We then sample a pair of subsets from the extracted keys and values, which we denote $K'_{t,m,n-1}$ and $V'_{t,m,n-1}$, respectively. The subsampled sets $K'_{t,m,n-1}$ and $V'_{t,m,n-1}$ are then injected to the self-attention operation for the temporally subsequent tile $x'_{t,m,n}$. Specifically, at each self-attention layer for $x'_{t,m,n}$, we construct new sets of keys and values $\hat{K}_{t,m,n}$ and $\hat{V}_{t,m,n}$ by merging $K_{t,m,n}$ and $K'_{t,m,n-1}$, and $V_{t,m,n}$ and $V'_{t,m,n-1}$, respectively. We perform the self-attention operations using the extended keys and values using Eq. (2). Similar to SAP, we apply the TAP scheme to the first two and last two spatial self-attention layers.

To sample $K'_{t,m,n-1}$ and $V'_{t,m,n-1}$, we select L frames whose keys have the largest standard deviations from tile $x'_{t,m,n-1}$. This selection is based on the observation that frames with more varied and sharp details produce distinct keys, leading to larger standard deviations. In our experiments, we set $L = 4$. We then use the keys and values from these samples as $K'_{t,m,n-1}$ and $V'_{t,m,n-1}$. For a detailed analysis of this sampling strategy, refer to the supplementary material.

3.3 Detail-Suppression Self-Attention Guidance

To improve the quality of VSR, DC-VSR adopts DSSAG. In this subsection, we first briefly review the previous guidance approaches: CFG [Ho and Salimans 2021], SAG [Hong et al. 2023], and PAG [Ahn et al. 2024]. We then describe DSSAG in detail.

CFG. To improve sampling quality, CFG [Ho and Salimans 2021] utilizes both a conditional noise and an unconditional noise for denoising at each sampling step. Specifically, CFG is defined as:

$$\epsilon_{\text{CFG}}(x_t) = \epsilon_\theta(x_t) + (1 + s)(\epsilon_\theta(x_t, c) - \epsilon_\theta(x_t)), \quad (3)$$

where x_t is a latent of a synthesized image at diffusion sampling step t , ϵ_θ is a denoising U-Net, which is parameterized by θ , s is the CFG scale parameter, and c is the class condition. Eq. (3) emphasizes the class-related components in the latent, resulting in the final synthesized image better reflecting the class condition c .

SAG. Both SAG [Hong et al. 2023] and PAG [Ahn et al. 2024] improve high-frequency details in synthesized images by introducing perturbation to the high-frequency details in the estimation of the unconditional noise. Specifically, a generalized form of the diffusion guidance can be defined as:

$$\epsilon_{\text{DG}}(x_t) = \epsilon_\theta(\hat{x}_t) + (1 + s)(\epsilon_\theta(\hat{x}_t, h_t) - \epsilon_\theta(\hat{x}_t)), \quad (4)$$

where h_t is a condition, and \hat{x}_t is a perturbed sample that lacks h_t . Based on this generalized form, SAG is defined as:

$$\epsilon_{\text{SAG}}(x_t) = \epsilon_\theta(b(x_t)) + (1 + s)(\epsilon_\theta(x_t) - \epsilon_\theta(b(x_t))), \quad (5)$$

where b is a blurring operation that detects local regions with high-frequency details using self-attention scores, and blurs the detected regions, while keeping the noise in x_t intact. The missing high-frequency details in $b(x_t)$ corresponds to h_t in Eq. (4), i.e., $h_t = x_t - b(x_t)$. Eq. (5) amplifies high-frequency details synthesized by the conditional model, eventually leading to synthesis results with higher-quality details. SAG applies blurring only to regions with

high-frequency details to keep image structure intact, as blurring the entire image may destroy image structures, causing synthesis results with inaccurate image structures.

PAG. PAG proposes a simpler approach, which is defined as:

$$\epsilon_{\text{PAG}}(x_t) = \epsilon_{\theta}^{\text{PAG}}(x_t) + (1+s)(\epsilon_{\theta}(x_t) - \epsilon_{\theta}^{\text{PAG}}(x_t)), \quad (6)$$

where $\epsilon_{\theta}^{\text{PAG}}(x_t)$ estimates noise from a perturbed version of x_t . To achieve this, PAG replaces the self-attention score matrix with an identity matrix in the self-attention layers in $\epsilon_{\theta}^{\text{PAG}}(x_t)$, i.e., it replaces the self-attention operations with $\text{SA}_{\text{perturb}}(\mathbf{Q}, \mathbf{K}, \mathbf{V}) = \mathbf{V}$. As a result, $\epsilon_{\theta}^{\text{PAG}}(x_t)$ does not leverage spatially distant information for noise estimation, estimating less accurate noise from x_t , which is analogous to noise estimation from a perturbed version of x_t .

SAG and PAG noticeably improve image synthesis quality, especially when combined with CFG. However, integrating them with CFG incurs substantial computational costs. While using $\epsilon_{\theta}(x_t, c)$ instead of $\epsilon_{\theta}(x_t)$ in Eqs. (5) and (6) allows this combination, it requires running the denoising U-Net three times for SAG, as it needs additional running of the denoising U-Net to detect high-frequency regions for the blurring operation. For PAG, the fixed level of perturbation complicates balancing the effects of CFG and PAG when combined. Consequently, PAG and CFG are typically applied separately, which also necessitates three runs of the denoising U-Net.

DSSAG. To enhance high-frequency details, DSSAG offers a simpler approach without additional computational costs. The core idea of DSSAG is as follows. As estimating noise from a noisy image is equivalent to estimating a noise-free image, we assume that the denoising U-Net of a diffusion model estimates a noise-free image in the following. For estimating a noise-free image, the self-attention layers in a denoising U-Net find image regions with similar high-frequency details, by computing weights based on the similarities between queries and keys. Then, they aggregate information from different image regions based on their weights. As noted by Wang *et al.* [2018a], this self-attention mechanism closely resembles bilateral filter [Tomasi and Manduchi 1998] and non-local means filter [Buades *et al.* 2005], both of which are renowned structure-preserving filters. Inspired by this, we introduce an additional parameter γ to control the weighting function of the self-attention operation, similar to the weighting parameters in bilateral and non-local means filters.

Specifically, we extend the self-attention operation as:

$$\text{SA}(\mathbf{Q}, \mathbf{K}, \mathbf{V}, \gamma) = \text{softmax}\left(\frac{\mathbf{Q}\mathbf{K}^{\top}}{\max(\gamma^2 qk, 1)\sqrt{d}}\right)\mathbf{V}, \quad (7)$$

where q and k represent the largest absolute values among the elements of \mathbf{Q} and \mathbf{K} , respectively. We adopt q and k to adaptively control the weights to the scales of the keys and values. $\max(\cdot, 1)$ is adopted to make Eq. (7) reduce to the conventional self-attention operation, when γ is small. Eq. (7) performs in a similar manner to the non-local means filter. Thanks to the similarity-based weighting function, it preserves salient image structures. Moreover, γ allows control over the blurring strength. Assigning a large value to γ results in larger weights for keys less similar to the queries, causing the information from different image regions to be more blended.

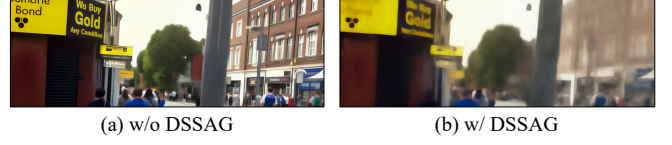


Fig. 3. Denoised results of unconditional term at the intermediate timestep ($t=16$ out of 25) (a) without and (b) with DSSAG. The input video is from the VideoLQ dataset [Chan *et al.* 2022b] (sample 013).

Consequently, the denoising U-Net estimates a blurrier image with fewer high-frequency details as shown in Fig. 3.

Leveraging the extended self-attention operation in Eq. (7), we define DSSAG and its combination with CFG as:

$$\epsilon_{\text{DSSAG}}(x_t) = \epsilon'_{\theta}(x_t) + (1+s)\left(\epsilon_{\theta}(x_t) - \epsilon'_{\theta}(x_t)\right) \quad \text{and} \quad (8)$$

$$\epsilon_{\text{CFG\&DSSAG}}(x_t) = \epsilon'_{\theta}(x_t) + (1+s)\left(\epsilon_{\theta}(x_t, c) - \epsilon'_{\theta}(x_t)\right), \quad (9)$$

where ϵ'_{θ} is a denoising U-Net whose self-attention operations are replaced with Eq. (7). ϵ'_{θ} does not require any training and shares the same parameters with ϵ_{θ} . DSSAG offers a couple of distinct benefits compared to SAG [Hong *et al.* 2023] and PAG [Ahn *et al.* 2024]. It does not need additional high-frequency detection or blurring operations, as Eq. (7) already incorporates these in its weighting and aggregation mechanism. Furthermore, DSSAG provides smooth control over blur strength, unlike PAG, enabling seamless integration with CFG without any additional computational costs.

We apply DSSAG to the first two and last two spatial self-attention layers in the denoising U-Net, as done for SAP and TAP. During the iterative sampling process of DC-VSR, we set γ adaptively to the noise level of the diffusion model, so that γ is initially large and gradually decreases as the sampling proceeds. Specifically, we set γ_t at diffusion sampling step t as:

$$\gamma_t = \left(\frac{\ln \sigma_t - \ln \sigma_T}{\ln \sigma_0 - \ln \sigma_T}\right)^{\rho}, \quad (10)$$

where σ_t is the noise level at t , and ρ is a parameter to control the detail suppression strength, which is set to 0.5 in our experiments.

4 EXPERIMENTS

To build DC-VSR, we fine-tune Image-to-Video Stable Video Diffusion (I2V-SVD) [StabilityAI 2023], which adopts the LDM framework [Rombach *et al.* 2022] with the EDM [Karras *et al.* 2022] diffusion mechanism. We use the REDS dataset [Nah *et al.* 2019] to train our model. Following previous work [Chan *et al.* 2022b; Yang *et al.* 2024a], we merge 240 training videos and 30 test videos, reorganizing them into 266 training videos and 4 test videos, and refer to the latter as REDS4. We refer the reader to the supplementary material for more implementation details.

We use the REDS4 [Chan *et al.* 2022b] and UDM10 [Yi *et al.* 2019] datasets for VSR evaluation. We construct HR-LR video pairs from the datasets using the real-world degradation pipeline of Chan *et al.* [2022b], which applies random blur, resizing, noise, JPEG compression, and video compression. Additionally, we use the VideoLQ dataset [Chan *et al.* 2022b] as a real-world LR dataset.

Table 1. Quantitative comparisons of different VSR (x4) models on synthetic datasets (REDS4 and UDM10) and real datasets (VideoLQ). ISR, VSR and GP are image super-resolution tasks, video super-resolution tasks and generative prior. The best and second-best scores are marked in **bold** and underline. DOVER* and tLP* denote DOVER ($\times 100$) and tLP ($\times 100$) respectively.

Datasets	Metrics	ISR w/o GP		ISR w/ GP		VSR w/o GP		VSR w/ GP		
		Bicubic	SwinIR	Real-ESRGAN	StableSR	RealBasicVSR	RealViformer	UAVideo	MGLD	DC-VSR
REDS4	PSNR \uparrow	25.92	24.55	24.22	23.81	25.49	26.40	24.32	25.57	25.11
	SSIM \uparrow	0.6910	0.6875	0.6796	0.6514	<u>0.7069</u>	0.7063	0.6494	0.6781	0.7106
	DISTS \downarrow	0.2571	0.1251	0.1335	0.1257	0.1120	0.1162	0.1506	0.0885	<u>0.1087</u>
	tOF \downarrow	2.91	2.65	2.51	2.82	<u>2.09</u>	2.19	2.65	3.48	2.01
	tLP* \downarrow	1.97	2.26	1.53	4.12	<u>0.85</u>	1.26	1.65	3.01	0.71
	MUSIQ \uparrow	24.71	64.54	64.86	<u>67.31</u>	65.65	63.67	57.06	65.20	69.22
	DOVER* \uparrow	11.91	57.80	61.00	58.97	64.43	65.94	57.06	<u>68.83</u>	70.41
UDM10	PSNR \uparrow	29.62	28.46	27.93	26.69	28.94	30.41	27.52	29.08	28.71
	SSIM \uparrow	0.8536	0.8546	0.8446	0.7975	0.8542	0.8633	0.7975	0.8485	<u>0.8550</u>
	DISTS \downarrow	0.1940	0.1230	0.1370	0.1565	0.1327	0.1274	0.1482	0.1168	<u>0.1220</u>
	tOF \downarrow	1.38	1.28	1.33	1.45	1.11	<u>1.09</u>	1.34	1.53	1.04
	tLP* \downarrow	1.79	2.78	2.77	5.06	1.21	<u>1.00</u>	1.81	1.93	0.94
	MUSIQ \uparrow	28.06	61.41	61.44	<u>65.88</u>	63.43	60.86	64.19	62.79	67.16
	DOVER* \uparrow	15.73	74.29	76.02	<u>77.28</u>	77.19	75.58	76.67	76.86	77.82
VideoLQ	MUSIQ \uparrow	22.58	50.34	49.84	54.17	55.96	52.13	48.02	51.37	58.14
	DOVER* \uparrow	38.92	72.32	71.61	71.14	73.80	71.75	70.17	<u>73.98</u>	78.31

4.1 Comparison with Previous SR and VSR Approaches

To evaluate the performance of DC-VSR, we compare it with various previous methods across different categories. Specifically, our evaluation includes non-generative image super-resolution (ISR) methods: bicubic interpolation and SwinIR [Liang et al. 2021]; two generative ISR methods: Real-ESRGAN [Wang et al. 2021] and StableSR [Wang et al. 2024]; two non-generative VSR methods: RealBasicVSR [Chan et al. 2022b] and RealViformer [Zhang and Yao 2024]; and two generative VSR methods: Upscale-A-Video (UAVideo) [Zhou et al. 2024] and MGLD [Yang et al. 2024a]. We follow the default settings from the official repositories of prior works in our experiments.

For quantitative evaluation on synthetic datasets that provide ground-truth HR videos, we use PSNR, SSIM, DISTS [Ding et al. 2021], tOF, and tLP [Chu et al. 2020]. PSNR, SSIM, and DISTS measure the quality of each frame in super-resolution results, while tOF and tLP measure the temporal consistency by comparing optical flows estimated from super-resolution results with ground-truth optical flows. We also conduct a quantitative evaluation on a real-world dataset, VideoLQ [Chan et al. 2022b], using no-reference quality metrics: MUSIQ [Xie et al. 2022] and DOVER [Wu et al. 2023]. MUSIQ measures perceptual image quality, while DOVER is a video quality metric that quantifies aesthetic quality and technical artifacts such as compression or blur.

Table 1 presents a quantitative comparison with previous methods. It is important to note that quantitatively measuring VSR quality is challenging, especially for generative-prior-based approaches, due to the synthesized details that may not align with the ground-truth details. Nevertheless, on both synthetic and real-world datasets, DC-VSR consistently demonstrates superior or comparable results across various metrics. For PSNR and SSIM, non-generative methods generally achieve higher scores as they do not synthesize high-frequency details that may not align with ground-truth videos. However, this often results in blurry outputs as will be shown in Figs. 7 to 9. Compared to previous generative VSR methods, DC-VSR achieves competitive PSNR scores and higher SSIM scores. When considering

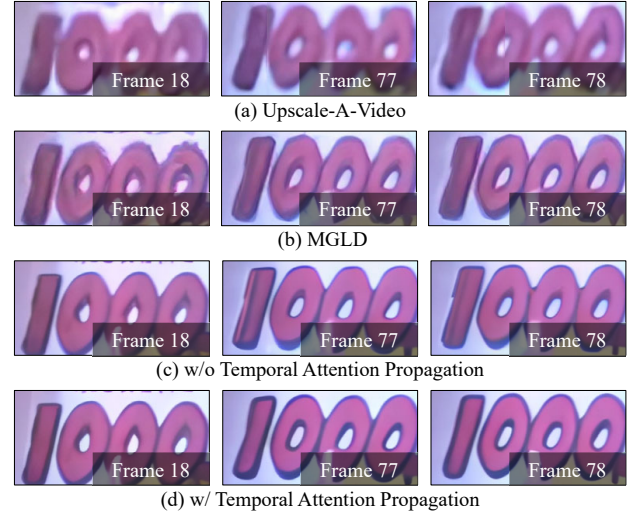


Fig. 4. (a)&(b) are VSR results of image diffusion prior-based methods. (c)&(d) show the effects on the proposed TAP. The input video is from the VideoLQ dataset [Chan et al. 2022b] (sample 008).

DISTS, a perceptual metric, DC-VSR ranks second among all methods. Regarding temporal consistency, measured by tOF and tLP, DC-VSR outperforms all other methods, including non-generative ones, highlighting the effectiveness of video generative prior and our TAP scheme. Finally, evaluating video quality independent of ground-truth data using MUSIQ and DOVER, DC-VSR outperforms other methods in most cases on both synthetic and real-world datasets.

Fig. 7 presents a qualitative comparison focusing on spatial consistency. Among the compared methods, RealViformer [Zhang and Yao 2024] processes the entire spatial area of video frames without splitting them into multiple spatial tiles. However, it lacks mechanisms, such as spatial attention, to ensure consistency between distant regions, resulting in spatially inconsistent artifacts. The other methods, including ours, adopt tile-based approaches. For all

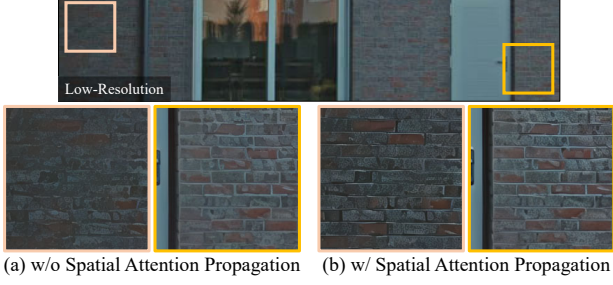


Fig. 5. Visualization of the effects on the proposed SAP. The input video is from Pexels (©Tima Miroshnichenko).

tile-based approaches, the regions marked by red squares in the LR frames belong to different tiles. As shown in the results, our method produces high-quality, spatially-consistent results despite our tile-based approach, surpassing the other approaches.

Fig. 8 presents a qualitative comparison focusing on temporal consistency. In the figure, all previous approaches exhibit challenges in producing temporally consistent HR details for both distant and neighboring frames. StableSR [Wang et al. 2024], an image super-resolution (ISR) approach, handles each video frame separately, which inherently limits its temporal consistency. RealViFormer [Zhang and Yao 2024] propagates information bidirectionally between neighboring frames, but this method still struggles with ensuring consistency across longer temporal sequences. Moreover, due to the lack of generative prior, its results show less realistic details. Meanwhile, MGLD [Yang et al. 2024a] and UAVideo [Zhou et al. 2024], both VSR approaches, rely on image diffusion priors and process temporal tiles, but struggle to maintain temporal consistency. Finally, our results show superior temporal consistency and higher-quality HR details than the results of previous methods.

Fig. 9 presents a qualitative comparison highlighting the restoration quality of a single frame, demonstrating the superiority of DC-VSR over previous methods. For example, DC-VSR excels at restoring building windows, adding plausible details to degraded regions, as seen in VideoLQ 020. Notably, it surpasses other VSR methods in restoring characters, a particularly challenging task for generative models, as seen in VideoLQ 049. These results indicate that DC-VSR not only ensures spatio-temporal consistency but also achieves outstanding restoration quality.

The superior performance of DC-VSR, demonstrated in Figs. 7 to 9, stems from the video diffusion prior and our proposed components. Specifically, the video diffusion prior leverages spatially and temporally distant information within a spatio-temporal tile, ensuring not only spatio-temporal consistency but also enhanced HR details. Furthermore, our SAP and TAP schemes allow exploiting information from distant tiles, further improving spatio-temporal consistency and HR details. Finally, our DSSAG scheme additionally improves the quality of HR details.

4.2 Component Evaluation

Effect of Video Diffusion Prior. Fig. 4(a-b) and (c) show the VSR results of previous methods utilizing image diffusion priors and our method employing video diffusion priors, respectively. While image diffusion prior-based methods incorporate additional techniques to

Table 2. Ablation study of SAP & TAP and comparison with previous guidance methods using the REDS4 dataset. DOVER* denotes DOVER ($\times 100$). The best and second-best scores are marked in **bold** and underline. Our proposed DSSAG is 1.5 \times faster than SAG and PAG.

SAP	TAP	DSSAG	SAG [2023]	PAG [2024]	MUSIQ \uparrow	DOVER* \uparrow
-	-	-	-	-	67.51	66.07
✓	-	-	-	-	67.52	66.10
-	✓	-	-	-	67.51	66.19
✓	✓	✓	-	-	<u>69.22</u>	70.41
✓	✓	-	✓	-	68.30	<u>69.43</u>
✓	✓	-	-	✓	71.24	68.55

enhance temporal consistency, they produce blurry and inconsistent outcomes. In contrast, our approach, which directly applies video diffusion priors without additional temporal consistency techniques, shows significantly clearer and more temporally consistent results.

Ablation Study on TAP & SAP. Fig. 4(c) and (d) present the VSR results without and with TAP, respectively. By applying TAP, temporal consistency between distant frames is effectively preserved. Specifically, in frame 77, a vertical line in the number “1” appears in (c) but remains absent in (d), maintaining the original consistency. Fig. 5 illustrates the VSR results of two distant brick regions in a frame, comparing outcomes without and with SAP, respectively. Without SAP, the brick patterns appear mismatched between the regions. In contrast, after applying SAP, the distant brick patterns are restored with coherent details. Additionally, the first three rows in Table 2 present ablation studies on SAP and TAP. Both schemes show improvements in the DOVER. In contrast, since MUSIQ measures image quality, no improvement is observed for TAP. For a detailed visualization of the enhancements brought by SAP and TAP, please refer to the supplemental video.

Comparisons with Guidance Methods. Fig. 6 presents qualitative comparisons of DSSAG with previous guidance approaches, where our method shows the clearest image quality and most accurate character shape. The last three rows in Table 2 provide quantitative comparisons, showing that DSSAG achieves the best performance in DOVER and the second-best in MUSIQ, while being 1.5 \times faster than previous methods. Moreover, since these guidance methods can be generally applicable beyond VSR, we provide additional comparisons for image generation in the supplemental document.

Effect of ρ in DSSAG. DSSAG adjusts the detail suppression strength using ρ . Fig. 10 shows the effect of ρ . A smaller ρ increases the blurring effect in Eq. (7), resulting in more enhanced edges. In contrast, a larger ρ makes Eq. (7) closer to the conventional self-attention operation, producing less enhanced but more accurate details. This flexibility allows our framework to adapt to various scenarios: a small ρ is suitable for severely degraded LR videos or animation videos, while a large ρ works better for mildly degraded LR videos.

5 CONCLUSION

In this paper, we introduced DC-VSR, a novel approach leveraging a video diffusion prior to produce spatially and temporally consistent VSR results with realistic textures. Our proposed SAP



Fig. 6. Qualitative comparison with previous guidance approaches. The input video is from the VideoLQ dataset [Chan et al. 2022b] (sample 041).

and TAP schemes effectively address the challenges of maintaining consistency across spatio-temporal tiles. Furthermore, our DSSAG provides high-frequency detail enhancement without incurring additional computational costs.

Limitations & Future Work. Since DC-VSR is based on a diffusion model, it may generate false details and face difficulties in achieving real-time VSR. Moreover, DC-VSR may struggle to maintain temporal consistency across distant temporal tiles in long video clips, as TAP primarily relies on nearby tiles. Addressing these issues could be a promising future direction.

ACKNOWLEDGMENTS

This work was supported by Samsung Electronics Co., Ltd., the Institute of Information & Communications Technology Planning & Evaluation (IITP) grants (RS-2019-II191906, Artificial Intelligence Graduate School Program (POSTECH), No.2021-0-02068, Artificial Intelligence Innovation Hub), and the National Research Foundation of Korea (NRF) grant (No.2018R1A5A1060031), funded by the Korea government (MSIT).

REFERENCES

Donghoon Ahn, Hyoungho Cho, Jaewon Min, Woosok Jang, Jungwoo Kim, Seon-Hwa Kim, Hyun Hee Park, Kyong Hwan Jin, and Seungryong Kim. 2024. Self-Rectifying Diffusion Sampling with Perturbed-Attention Guidance. *arXiv preprint arXiv:2403.17377* (2024).

Omer Bar-Tal, Lior Yariv, Yaron Lipman, and Tali Dekel. 2023. MultiDiffusion: Fusing Diffusion Paths for Controlled Image Generation. *arXiv preprint arXiv:2302.08113* (2023).

Andreas Blattmann, Tim Dockhorn, Sumith Kulal, Daniel Mendelevitch, Maciej Kilian, Dominik Lorenz, Yam Levi, Zion English, Vikram Voleti, Adam Letts, Varun Jampani, and Robin Rombach. 2023a. Stable Video Diffusion: Scaling Latent Video Diffusion Models to Large Datasets. *arXiv:2311.15127 [cs.CV]* <https://arxiv.org/abs/2311.15127>

Andreas Blattmann, Robin Rombach, Huan Ling, Tim Dockhorn, Seung Wook Kim, Sanja Fidler, and Karsten Kreis. 2023b. Align your Latents: High-Resolution Video Synthesis with Latent Diffusion Models. In *IEEE Conference on Computer Vision and Pattern Recognition (CVPR)*.

Antoni Buades, Bartomeu Coll, and J-M Morel. 2005. A non-local algorithm for image denoising. In *2005 IEEE computer society conference on computer vision and pattern recognition (CVPR'05)*, Vol. 2. Ieee, 60–65.

Kelvin CK Chan, Xintao Wang, Ke Yu, Chao Dong, and Chen Change Loy. 2021. BasicVSR: The Search for Essential Components in Video Super-Resolution and Beyond. In *IEEE Conference on Computer Vision and Pattern Recognition (CVPR)*.

Kelvin C.K. Chan, Shangchen Zhou, Xiangyu Xu, and Chen Change Loy. 2022a. BasicVSR++: Improving video super-resolution with enhanced propagation and alignment. In *IEEE Conference on Computer Vision and Pattern Recognition (CVPR)*.

Kelvin C.K. Chan, Shangchen Zhou, Xiangyu Xu, and Chen Change Loy. 2022b. Investigating Tradeoffs in Real-World Video Super-Resolution. In *IEEE Conference on Computer Vision and Pattern Recognition (CVPR)*.

Kelvin C. K. Chan, Xintao Wang, Xiangyu Xu, Jinwei Gu, and Chen Change Loy. 2020. GLEAN: Generative Latent Bank for Large-Factor Image Super-Resolution. *arXiv:2012.00739 [cs.CV]* <https://arxiv.org/abs/2012.00739>

Zhikai Chen, Fuchen Long, Zhaofan Qiu, Ting Yao, Wengang Zhou, Jiebo Luo, and Tao Mei. 2024. Learning Spatial Adaptation and Temporal Coherence in Diffusion Models for Video Super-Resolution. In *IEEE Conference on Computer Vision and Pattern Recognition (CVPR)*.

Mengyu Chu, You Xie, Jonas Mayer, Laura Leal-Taixé, and Nils Thuerey. 2020. Learning temporal coherence via self-supervision for GAN-based video generation. *ACM Trans. Graph.* 39, 4 (Aug. 2020). <https://doi.org/10.1145/3386569.3392457>

CompVis. 2022. Stable Diffusion v1.4. <https://huggingface.co/CompVis/stable-diffusion-v1-4>

Keyan Ding, Kede Ma, Shiqi Wang, and Eero P. Simoncelli. 2021. Image Quality Assessment: Unifying Structure and Texture Similarity. *IEEE Transactions on Pattern Analysis and Machine Intelligence* (2021). <https://doi.org/10.1109/TPAMI.2020.3045810>

Chao Dong, Chen Change Loy, Kaiming He, and Xiaoou Tang. 2015. Image Super-Resolution Using Deep Convolutional Networks. *arXiv:1501.00092 [cs.CV]* <https://arxiv.org/abs/1501.00092>

Ruoyi Du, Dongliang Chang, Timothy Hospedales, Yi-Zhe Song, and Zhanyu Ma. 2024. DemoFusion: Democratising High-Resolution Image Generation With No \$\$\$ In *CVPR*.

Abhijay Ghildyal and Feng Liu. 2022. Shift-tolerant Perceptual Similarity Metric. In *European Conference on Computer Vision*.

Ian J. Goodfellow, Jean Pouget-Abadie, Mehdi Mirza, Bing Xu, David Warde-Farley, Sherjil Ozair, Aaron Courville, and Yoshua Bengio. 2014. Generative Adversarial Networks. *arXiv:1406.2661 [stat.ML]* <https://arxiv.org/abs/1406.2661>

Muhammad Haris, Greg Shakhnarovich, and Norimichi Ukita. 2018. Deep Back-Projection Networks For Super-Resolution. *arXiv:1803.02735 [cs.CV]* <https://arxiv.org/abs/1803.02735>

Martin Heusel, Hubert Ramsauer, Thomas Unterthiner, Bernhard Nessler, and Sepp Hochreiter. 2018. GANs Trained by a Two Time-Scale Update Rule Converge to a Local Nash Equilibrium. *arXiv:1706.08500 [cs.LG]* <https://arxiv.org/abs/1706.08500>

Jonathan Ho and Tim Salimans. 2021. Classifier-Free Diffusion Guidance. In *Conference on Neural Information Processing Systems (NeurIPS)*.

Susung Hong, Gyuseong Lee, Woosok Jang, and Seungryong Kim. 2023. Improving Sample Quality of Diffusion Models Using Self-Attention Guidance. In *International Conference on Computer Vision (ICCV)*.

Tero Karras, Miika Aittala, Timo Aila, and Samuli Laine. 2022. Elucidating the Design Space of Diffusion-Based Generative Models. In *Conference on Neural Information Processing Systems (NeurIPS)*.

Jiwon Kim, Jung Kwon Lee, and Kyoung Mu Lee. 2016a. Accurate Image Super-Resolution Using Very Deep Convolutional Networks. *arXiv:1511.04587 [cs.CV]* <https://arxiv.org/abs/1511.04587>

Jiwon Kim, Jung Kwon Lee, and Kyoung Mu Lee. 2016b. Deeply-Recursive Convolutional Network for Image Super-Resolution. *arXiv:1511.04491 [cs.CV]* <https://arxiv.org/abs/1511.04491>

Wei-Sheng Lai, Jia-Bin Huang, Narendra Ahuja, and Ming-Hsuan Yang. 2017. Deep Laplacian Pyramid Networks for Fast and Accurate Super-Resolution. *arXiv:1704.03915 [cs.CV]* <https://arxiv.org/abs/1704.03915>

Christian Ledig, Lucas Theis, Ferenc Huszar, Jose Caballero, Andrew Cunningham, Alejandro Acosta, Andrew Aitken, Alykhan Tejani, Johannes Totz, Zehan Wang, and Wenzhe Shi. 2017. Photo-Realistic Single Image Super-Resolution Using a Generative Adversarial Network. *arXiv:1609.04802 [cs.CV]* <https://arxiv.org/abs/1609.04802>

Yuseung Lee, Kunho Kim, Hyunjin Kim, and Minhyuk Sung. 2023. SyncDiffusion: Coherent Montage via Synchronized Joint Diffusions. In *Thirty-seventh Conference on Neural Information Processing Systems*.

Jingyun Liang, Jiezhang Cao, Guolei Sun, Kai Zhang, Luc Van Gool, and Radu Timofte. 2021. SwinIR: Image Restoration Using Swin Transformer. In *International Conference on Computer Vision Workshops (ICCVW)*.

Tsung-Yi Lin, Michael Maire, Serge Belongie, Lubomir Bourdev, Ross Girshick, James Hays, Pietro Perona, Deva Ramanan, C. Lawrence Zitnick, and Piotr Dollár. 2015. Microsoft COCO: Common Objects in Context. *arXiv:1405.0312 [cs.CV]* <https://arxiv.org/abs/1405.0312>

Xinqi Lin, Jingwen He, Ziyang Chen, Zhaoyang Lyu, Bo Dai, Fanghua Yu, Wanli Ouyang, Yu Qiao, and Chao Dong. 2024. DiffBIR: Towards Blind Image Restoration with Generative Diffusion Prior. *arXiv:2308.15070 [cs.CV]*

Ilya Loshchilov and Frank Hutter. 2019. Decoupled Weight Decay Regularization. In *International Conference on Learning Representations*. <https://arxiv.org/abs/1711.05101>

Sachit Menon, Alexandru Damian, Shijia Hu, Nikhil Ravi, and Cynthia Rudin. 2020. PULSE: Self-Supervised Photo Upsampling via Latent Space Exploration of Generative Models. *arXiv:2003.03808 [cs.CV]* <https://arxiv.org/abs/2003.03808>

Seungjun Nah, Sungyong Baik, Seokil Hong, Gyeongsik Moon, Sanghyun Son, Radu Timofte, and Kyoung Mu Lee. 2019. NTIRE 2019 Challenge on Video Deblurring and Super-Resolution: Dataset and Study. In *CVPR Workshops*.

- Alec Radford, Jong Wook Kim, Chris Hallacy, Aditya Ramesh, Gabriel Goh, Sandhini Agarwal, Girish Sastry, Amanda Askell, Pamela Mishkin, Jack Clark, Gretchen Krueger, and Ilya Sutskever. 2021. Learning Transferable Visual Models From Natural Language Supervision. arXiv:2103.00020 [cs.CV] <https://arxiv.org/abs/2103.00020>
- Robin Rombach, Andreas Blattmann, Dominik Lorenz, Patrick Esser, and Björn Ommer. 2022. High-Resolution Image Synthesis with Latent Diffusion Models. In *IEEE Conference on Computer Vision and Pattern Recognition (CVPR)*.
- Claudio Rota, Marco Buzzelli, and Joost van de Weijer. 2024. Enhancing Perceptual Quality in Video Super-Resolution through Temporally-Consistent Detail Synthesis using Diffusion Models. In *The European Conference on Computer Vision (ECCV)*.
- Tim Salimans, Ian Goodfellow, Wojciech Zaremba, Vicki Cheung, Alec Radford, and Xi Chen. 2016. Improved Techniques for Training GANs. arXiv:1606.03498 [cs.LG] <https://arxiv.org/abs/1606.03498>
- StabilityAI. 2023. Stable Video Diffusion Image-to-Video. <https://huggingface.co/stabilityai/stable-video-diffusion-img2vid>
- Lingchen Sun, Rongyuan Wu, Zhengqiang Zhang, Hongwei Yong, and Lei Zhang. 2024. Improving the Stability of Diffusion Models for Content Consistent Super-Resolution. *arXiv preprint arXiv:2401.00877* (2024).
- Ying Tai, Jian Yang, and Xiaoming Liu. 2017. Image Super-Resolution via Deep Recursive Residual Network. In *2017 IEEE Conference on Computer Vision and Pattern Recognition (CVPR)*, 2790–2798. <https://doi.org/10.1109/CVPR.2017.298>
- Zachary Teed and Jia Deng. 2020. RAFT: Recurrent All-Pairs Field Transforms for Optical Flow. In *European Conference on Computer Vision (ECCV)*.
- Carlo Tomasi and Roberto Manduchi. 1998. Bilateral filtering for gray and color images. In *Sixth international conference on computer vision (IEEE Cat. No. 98CH36271)*. IEEE, 839–846.
- Jianyi Wang, Zongsheng Yue, Shangchen Zhou, Kelvin C.K. Chan, and Chen Change Loy. 2024. Exploiting Diffusion Prior for Real-World Image Super-Resolution. (2024).
- Xiaolong Wang, Ross Girshick, Abhinav Gupta, and Kaiming He. 2018a. Non-local neural networks. In *Proceedings of the IEEE conference on computer vision and pattern recognition*. 7794–7803.
- Xintao Wang, Liangbin Xie, Chao Dong, and Ying Shan. 2021. Real-ESRGAN: Training Real-World Blind Super-Resolution with Pure Synthetic Data. In *International Conference on Computer Vision Workshops (ICCVW)*.
- Xintao Wang, Ke Yu, Shixiang Wu, Jinjin Gu, Yihao Liu, Chao Dong, Chen Change Loy, Yu Qiao, and Xiaoou Tang. 2018b. ESRGAN: Enhanced Super-Resolution Generative Adversarial Networks. arXiv:1809.00219 [cs.CV] <https://arxiv.org/abs/1809.00219>
- Haoning Wu, Erli Zhang, Liang Liao, Chaofeng Chen, Jingwen Hou Hou, Annan Wang, Wenxiu Sun Sun, Qiong Yan, and Weisi Lin. 2023. Exploring Video Quality Assessment on User Generated Contents from Aesthetic and Technical Perspectives. In *International Conference on Computer Vision (ICCV)*.
- Rongyuan Wu, Lingchen Sun, Zhiyuan Ma, and Lei Zhang. 2024a. One-Step Effective Diffusion Network for Real-World Image Super-Resolution. *arXiv preprint arXiv:2406.08177* (2024).
- Rongyuan Wu, Tao Yang, Lingchen Sun, Zhengqiang Zhang, Shuai Li, and Lei Zhang. 2024b. Seesr: Towards semantics-aware real-world image super-resolution. In *Proceedings of the IEEE/CVF conference on computer vision and pattern recognition*. 25456–25467.
- Liangbin Xie, Xintao Wang, Shuwei Shi, Jinjin Gu, Chao Dong, and Ying Shan. 2023. Mitigating Artifacts in Real-World Video Super-Resolution Models. In *Association for the Advancement of Artificial Intelligence (AAAI)*.
- Yujia Xie, Yujun Shen, Zhiwei Xie, Yichen Wei, and Alan Yuille. 2022. MUSIQ: Learning Multimodal Representations for Visual Question Answering. In *Proceedings of the IEEE/CVF Conference on Computer Vision and Pattern Recognition (CVPR)*.
- Yiran Xu, Taesung Park, Richard Zhang, Yang Zhou, Eli Shechtman, Feng Liu, Jia-Bin Huang, and Difan Liu. 2024. VideoGigaGAN: Towards Detail-rich Video Super-Resolution. (2024). arXiv:2404.12388 [cs.CV]
- Tao Yang, Rongyuan Wu, Peiran Ren, Xuansong Xie, and Lei Zhang. 2024b. Pixel-Aware Stable Diffusion for Realistic Image Super-resolution and Personalized Stylization. arXiv:2308.14469 [cs.CV] <https://arxiv.org/abs/2308.14469>
- Xi Yang, Chenhang He, Jianqi Ma, and Lei Zhang. 2024a. Motion-Guided Latent Diffusion for Temporally Consistent Real-world Video Super-resolution. In *European Conference on Computer Vision (ECCV)*.
- Peng Yi, Zhongyuan Wang, Kui Jiang, Junjun Jiang, and Jiayi Ma. 2019. Progressive Fusion Video Super-Resolution Network via Exploiting Non-Local Spatio-Temporal Correlations. In *IEEE International Conference on Computer Vision (ICCV)*. 3106–3115.
- Geunhyuk Youk, Jihyong Oh, and Munchurl Kim. 2024. FMA-Net: Flow-Guided Dynamic Filtering and Iterative Feature Refinement with Multi-Attention for Joint Video Super-Resolution and Deblurring. In *IEEE Conference on Computer Vision and Pattern Recognition (CVPR)*.
- Fanghua Yu, Jinjin Gu, Zheyuan Li, Jinfan Hu, Xiangtao Kong, Xintao Wang, Jingwen He, Yu Qiao, and Chao Dong. 2024. Scaling Up to Excellence: Practicing Model Scaling for Photo-Realistic Image Restoration In the Wild. arXiv:2401.13627 [cs.CV]
- Richard Zhang, Phillip Isola, Alexei A Efros, Eli Shechtman, and Oliver Wang. 2018a. The Unreasonable Effectiveness of Deep Features as a Perceptual Metric. In *CVPR*.
- Yulun Zhang, Kunpeng Li, Kai Li, Lichen Wang, Bineng Zhong, and Yun Fu. 2018b. Image Super-Resolution Using Very Deep Residual Channel Attention Networks. arXiv:1807.02758 [cs.CV] <https://arxiv.org/abs/1807.02758>
- Yulun Zhang, Yapeng Tian, Yu Kong, Bineng Zhong, and Yun Fu. 2018c. Residual Dense Network for Image Super-Resolution. arXiv:1802.08797 [cs.CV] <https://arxiv.org/abs/1802.08797>
- Yuehan Zhang and Angela Yao. 2024. RealViformer: Investigating Attention for Real-World Video Super-Resolution. In *European Conference on Computer Vision (ECCV)*.
- Shangchen Zhou, Peiqing Yang, Jianyi Wang, Yihang Luo, and Chen Change Loy. 2024. Upscale-A-Video: Temporal-Consistent Diffusion Model for Real-World Video Super-Resolution. In *IEEE Conference on Computer Vision and Pattern Recognition (CVPR)*.

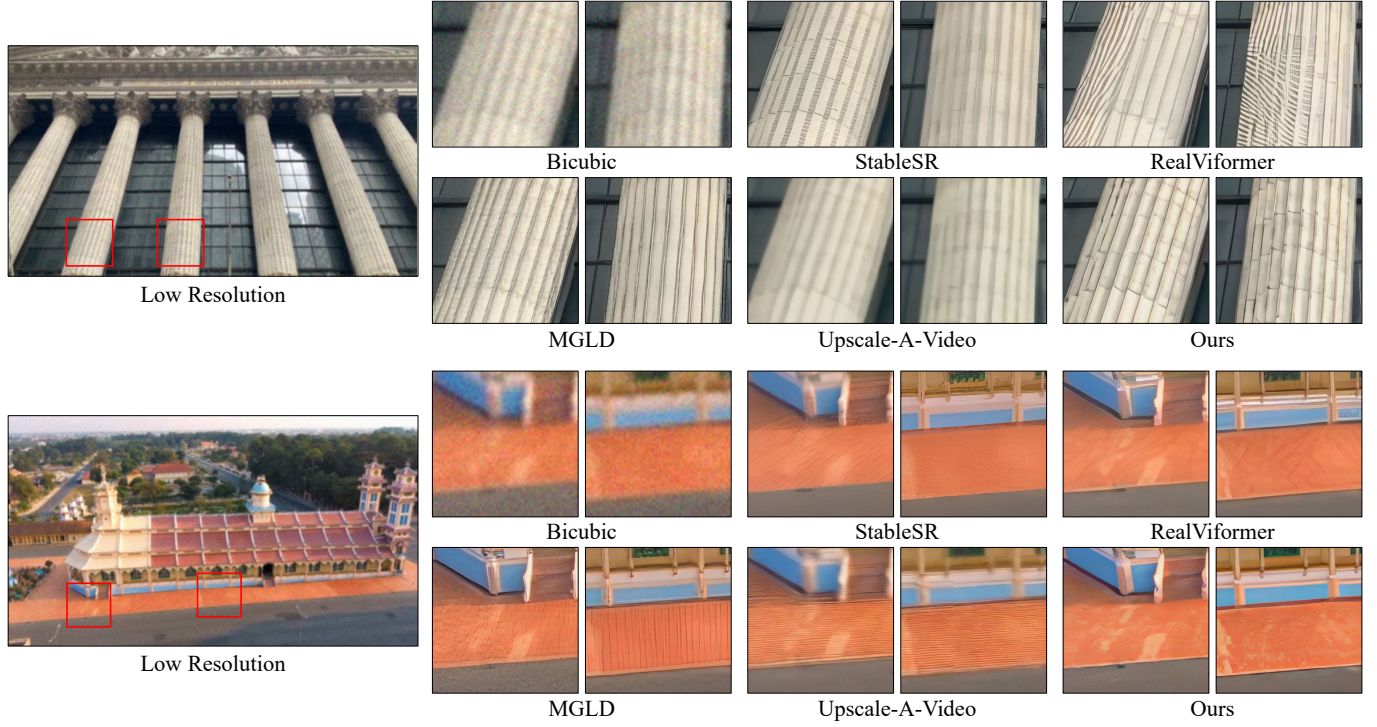


Fig. 7. Qualitative comparison of VSR (x4) with other state-of-the-art methods. Our proposed Spatial Attention Propagation (SAP) restores two spatial regions with consistent details and high quality. The input videos are from Pexels (©CityXcape, ©lam loi).



Fig. 8. Qualitative comparison of VSR (x4) with other state-of-the-art methods. Our proposed Temporal Attention Propagation (TAP) restores consecutive and distant frames with consistent details and high quality. The input videos are from the VideoLQ dataset [Chan et al. 2022b] (samples 007 and 036).

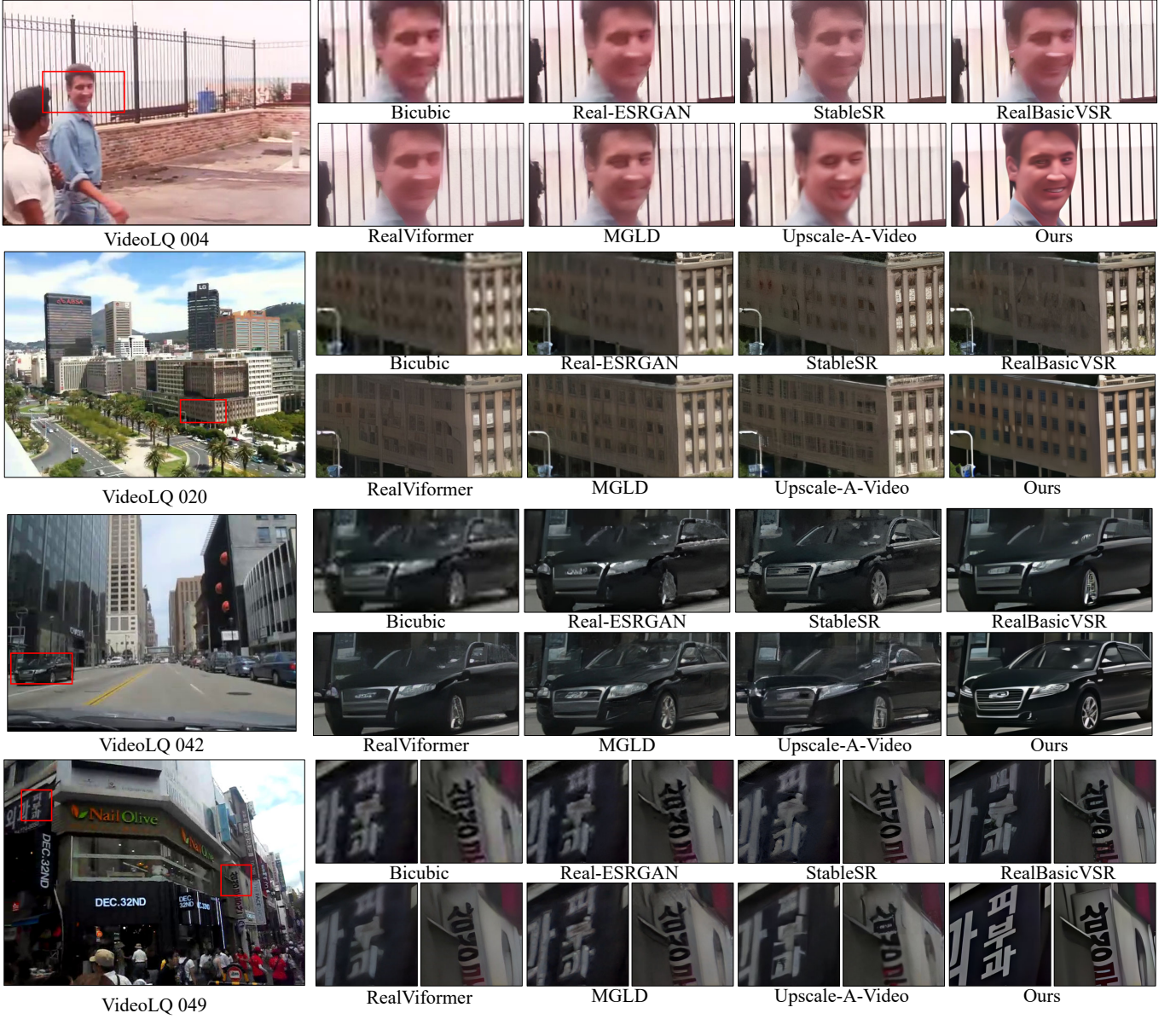


Fig. 9. Qualitative comparison of VSR (x4) on the real-world video dataset (VideoLQ) [Chan et al. 2022b] with other state-of-the-art methods. The input videos are from the VideoLQ dataset [Chan et al. 2022b].

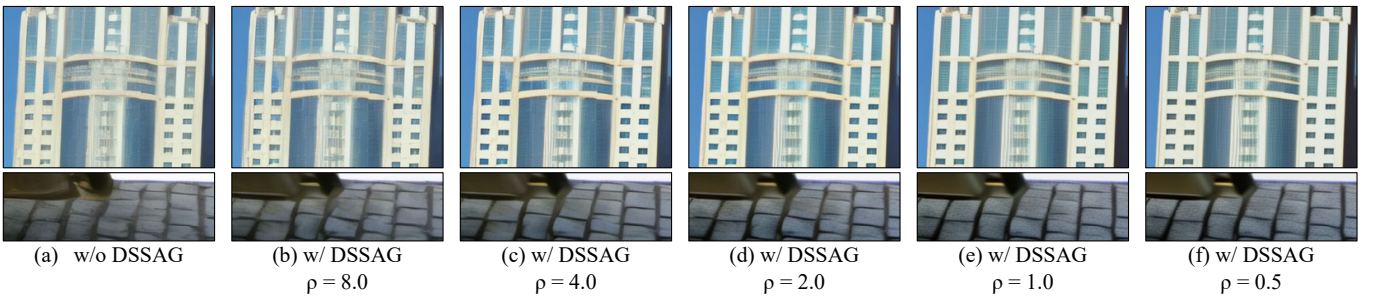


Fig. 10. Effects of ρ in DSSAG. (a) and (b)-(f) are the results of DC-VSR without and with DSSAG. The ability to refine and enhance high-frequency increases as the ρ value decreases. The input videos are from the VideoLQ dataset [Chan et al. 2022b] (samples 024 and 037).

SUPPLEMENTARY MATERIAL

We uploaded a [video](#) as Supplementary Material, containing VSR results and comparisons that include the contents mentioned in the main paper.

A IMPLEMENTATION DETAILS

We fine-tune Image-to-Video Stable Video Diffusion (I2V-SVD) [StabilityAI 2023] with an $8\times$ downsampling VAE [Rombach et al. 2022], trained on 14-frame sequences at a resolution of 576×1024 . We train DC-VSR using the AdamW optimizer [Loshchilov and Hutter 2019] with a learning rate of 1×10^{-4} and a batch size of 256 on four NVIDIA A100-80GB GPUs. Due to the memory limit, we use gradient accumulation to match the size of the batch. The training data are cropped into spatio-temporal tiles with width, height, and sequence length set to 512, 512, and 14, respectively. The denoising U-Net receives motion magnitude and a frame rate, fixed at 127 and 8, respectively, as conditioning inputs. Additionally, the denoising U-Net takes a CLIP [Radford et al. 2021] embedding vector of the first frame of the low-resolution input video as a text prompt. We initialize VAE and U-Net network parameters to pre-trained I2V-SVD [StabilityAI 2023] parameters. During training, we freeze the VAE and fine-tune all U-Net parameters for the first 5K iterations. Afterward, we fix the temporal attention and temporal residual block layers in the U-Net and fine-tune the U-Net for additional 5K iterations.

In our framework, Spatial Attention Propagation (SAP), Temporal Attention Propagation (TAP) and Detail-Suppression Self-Attention Guidance (DSSAG) are adopted to every spatial self-attention layer in the first two down-blocks and the last two up-blocks in the denoising U-Net. Merged keys and values in SAP and TAP are computed by concatenating each key and value along a flattened spatial dimension in the self-attention mechanism. In our experimental settings, DC-VSR is capable of performing video super-resolution ($\times 4$) on input videos of up to 768×768 resolution with 21 frames in a single NVIDIA A100-80GB GPU.

B ALTERNATING AND SIMULTANEOUS STRATEGIES FOR SAP AND TAP

While SAP and TAP may be applied simultaneously, our approach adopts an alternating application strategy to improve computational efficiency. Table 3 provides a performance comparison of the two approaches on the VideoLQ [Chan et al. 2022b] dataset. Both approaches show similar performance in MUSIQ [Xie et al. 2022] and DOVER* [Wu et al. 2023], but the simultaneous approach requires twice the inference time of the alternating approach. Therefore, we adopt the alternate approach in our proposed DC-VSR to ensure computational efficiency.

C SAMPLING STRATEGY FOR TAP

In this section, we show the effectiveness of our sampling strategy for TAP. Within the TAP scheme, we reduce the computational cost by selecting 4 frames from the previous spatial tile, which consists of 14 frames. A straightforward approach is to select frames randomly. However, we opt for a more informed strategy: selecting frames whose keys exhibit large standard deviations. This choice is based

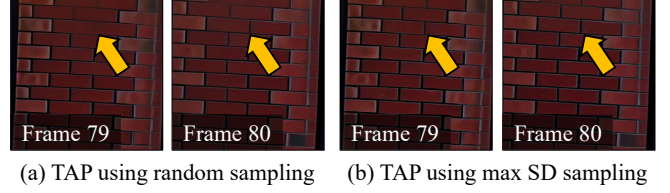


Fig. 11. Comparison of two different TAP sampling strategy. The input video is from the VideoLQ dataset [Chan et al. 2022b] (sample 013).

Table 3. Comparison of alternating and simultaneous application of SAP and TAP on the VideoLQ [Chan et al. 2022b] dataset. The best and second-best scores are marked in **bold** and underline.

Approach	Alternating	Simultaneous
MUSIQ \uparrow	58.15	<u>58.14</u>
DOVER* \uparrow	<u>78.30</u>	78.31

Table 4. Warping error (WE) as a function of the tile propagation range of TAP on the VideoLQ [Chan et al. 2022b] datasets (no.40–49). The best and second-best scores are marked in **bold** and underline, respectively.

# Tiles	1	2	3	4
WE \downarrow	0.1749	0.1744	<u>0.1745</u>	0.1746

on the observation that frames with more varied and sharper details tend to produce distinct keys, resulting in larger standard deviations. Fig. 11 illustrates this trend by comparing random sampling with maximum standard deviation (max SD) sampling. As shown, max SD sampling produces consistent and detailed brick patterns, in contrast to random sampling. This demonstrates that selecting detail-rich frames based on their standard deviations enhances the quality and consistency of temporal tiles.

D TILE PROPAGATION RANGE OF TAP

In TAP, temporal information is propagated bidirectionally from both the previous and next tiles. While increasing the propagation range can further enhance temporal consistency, it also introduces higher computational overhead and raises the risk of propagating inconsistent information. Table 4 compares the impact of different propagation ranges in terms of warping error (WE). The results indicate that increasing the propagation range does not lead to significant performance improvements, as the directly adjacent tiles already provide sufficient information for TAP. Furthermore, although a propagation range of 2 achieves the best performance, further extending the range degrades performance due to the propagation of inconsistent information between distant tiles. In our experiments, we adopt a propagation range of 1, as the performance improvement from additional tiles is minimal compared to the substantial increase in memory usage, requiring 3.2GB of GPU memory per tile.

Table 5. Performance comparison based on SAP subsampling rates. The best and second-best scores are marked in **bold** and underline, respectively.

Subsampling rate	8 (12.5%)	4 (25%)	2 (50%)	1 (100%)
LPIPS ↓	0.4693	0.4551	<u>0.4416</u>	0.4303
ST-LPIPS ↓	0.3065	0.2846	<u>0.2641</u>	0.2598
CLIP Similarity ↑	0.9500	0.9574	<u>0.9618</u>	0.9637

Table 6. Performance comparison based on TAP subsampling rates. The top row represents the number of subsampled key-value pairs out of 14 key-value pairs from the previous temporal tile. The best and second-best scores are marked in **bold** and underline, respectively.

# key-value pairs	1	2	4	8
WE ↓	0.1767	0.1758	<u>0.1749</u>	0.1742

E SUBSAMPLING RATES OF SAP AND TAP

SAP and TAP leverage subsampled information from the current frame and previous temporal tile to improve spatial and temporal consistency. A low subsampling rate, which preserves more information, can lead to improved performance, but significant computational costs are required. Table 5 shows correlation between subsampling rates and performance changes in SAP. We compare the average similarity over 28 frames between two distant spatial tiles, as indicated in Fig. 5 of our main paper. As the subsampling rate decreases, LPIPS [Zhang et al. 2018a], ST-LPIPS [Ghildyal and Liu 2022], and CLIP similarity [Radford et al. 2021] scores improve, indicating the performance increase. Consequently, utilizing the full information from the current frame (100% in Table 5) yields the best results.

Table 6 shows warping error (WE) under varying subsampling rates of TAP on the VideoLQ [Chan et al. 2022b] dataset (no.40-49). Similar to the trend in SAP, sampling more key-value pairs, which correspond to more extensive use of previous tile information, enhance temporal consistency. In our experimental settings, we select the subsampling rate of 2 for SAP, and 4 key-value pairs for TAP, which correspond to 50% and 28% sampling, respectively, considering computational overhead and performance improvement.

F ABLATION STUDY OF DSSAG

Fig. 12 demonstrates the effectiveness of DSSAG by comparing VSR results with and without DSSAG. Without DSSAG in Fig. 12, the car grille and the bases of the windows exhibit significant distortions. However, after applying DSSAG, these elements are restored with clear and precise details. These results highlight the effectiveness of DSSAG in enhancing visual quality and structural fidelity in VSR.

G IMAGE GENERATION COMPARISON OF DSSAG

The guidance methods, such as SAG [Hong et al. 2023], PAG [Ahn et al. 2024], and our DSSAG, are generally applicable to the diffusion sampling process. To demonstrate the general effectiveness of DSSAG, we compare the proposed method with SAG and PAG in the image generation task. Specifically, we generate 10K images using Stable Diffusion [CompVis 2022] and evaluate them using the

Inception Score (IS) [Salimans et al. 2016] and Fréchet Inception Distance (FID) [Heusel et al. 2018] metrics. The MS-COCO 2014 validation dataset [Lin et al. 2015] is used for these measurements. Table 7 presents the comparison. The proposed method achieves the best FID score and a comparable IS score, highlighting the general effectiveness of DSSAG. Notably, this performance is achieved with a 1.5× faster inference speed. Fig. 13 shows visualization of previous diffusion guidance approaches and DSSAG. DSSAG effectively improves image synthesis quality and integrates well with CFG.

H INFERENCE TIME COMPARISON

Table 8 presents a computation time comparison of diffusion-based video super-resolution methods for 4× super-resolution of 640×360 videos. Although DC-VSR significantly outperforms the previous approaches, it incurs slightly higher computational overhead, mainly due to the need for spatio-temporal tile splitting and merging at each diffusion timestep and attention-based approaches for maintaining spatial and temporal consistency.

I IMAGE-TO-VIDEO STABLE VIDEO DIFFUSION

I2V-SVD employs LDM [Rombach et al. 2022] structure with EDM [Karras et al. 2022] diffusion mechanism, which downsamples (x8) input with VAE encoder \mathcal{E} and proceeds continuous time diffusion denoising process in latent space. After the denoising process ended, it upsamples (x8) latent vectors with VAE decoder \mathcal{D} to the original RGB space. For training EDM with the LDM structure, diffusion loss can be defined as:

$$L(\theta) = \mathbb{E}_{\sigma, \mathbf{y}, \mathbf{n}} [\lambda(\sigma) \|D_{\theta}(\mathbf{y} + \mathbf{n}, \mathbf{c}, \sigma) - \mathbf{y}\|_2^2], \quad (11)$$

where D_{θ} is a denoiser network, \mathbf{c} is additional conditions such as text prompt, motion magnitude, and frame rate, σ is sampled noise level from predefined $p_{train}(\sigma)$, $\mathbf{y} \sim p_{\mathcal{E}(data)}$, $\mathbf{n} \sim \mathcal{N}(\mathbf{0}, \sigma^2 \mathbf{I})$ and $\lambda(\sigma)$ is adaptive loss weight. Here, CLIP [Radford et al. 2021] embedding vectors of the input image is given as text prompt. For stable and consistent input and output signal magnitudes, D_{θ} is derived from network F_{θ} in the following form:

$$D_{\theta}(\mathbf{x}, \mathbf{c}, \sigma) = c_{skip}(\sigma) \mathbf{x} + c_{out}(\sigma) F_{\theta}(c_{in}(\sigma) \mathbf{x}, \mathbf{c}, c_{noise}(\sigma)), \quad (12)$$

where $c_{skip}(\sigma)$, $c_{out}(\sigma)$, $c_{in}(\sigma)$ and $c_{noise}(\sigma)$ are parameterized function over the noise level σ and $\mathbf{x} = \mathbf{y} + \mathbf{n}$. In the sampling stage, noise levels $\sigma_{0 \sim T}$ are selected in the range $[0.002, 700]$ in descending order, and the deterministic diffusion backward process is calculated by solving ordinary differential equations from $\mathbf{x}_0 \sim \mathcal{N}(\mathbf{0}, 700^2 \mathbf{I})$ to \mathbf{x}_T , where T is the number of sampling time steps.

J TLP AND TOF

In [Chu et al. 2020], pixel-level video flows tOF and perceptual video flows tLP are respectively defined as:

$$tOF = \sum_{i=1}^L \|OF(\hat{g}_{i-1}, \hat{g}_i) - OF(g_{i-1}, g_i)\|_1, \quad (13)$$

$$tLP = \sum_{i=1}^L \|LPIPS(\hat{g}_{i-1}, \hat{g}_i) - LPIPS(g_{i-1}, g_i)\|_1, \quad (14)$$

where g_i is i -th frame of ground truth video, \hat{g}_i is i -th frame of restored video, $OF(\cdot)$ is optical flow estimator and $LPIPS(\cdot)$ is LPIPS

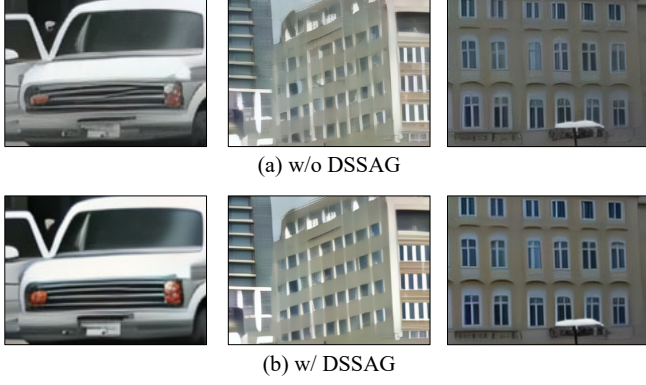


Fig. 12. Effects of DSSAG. The first row and second row are the results of DC-VSR without and with DSSAG. The proposed method enhances the generation quality of video frames. The input videos are from the VideoLQ dataset [Chan et al. 2022b] (sample 024, 039, and, 042).

Table 7. Comparisons with previous guidance methods using Inception Score (IS) [Salimans et al. 2016] and Fréchet Inception Distance (FID) [Heusel et al. 2018] metrics. feed-forward/iter. indicates the number of feed-forward passes required by the diffusion model for each denoising iteration. The best and second-best scores are marked in **bold** and underline.

Metrics	SAG [2023]	PAG [2024]	DSSAG
IS \uparrow	33.70	36.76	<u>36.04</u>
FID \downarrow	16.31	<u>16.27</u>	15.20
feed-forward/iter. \downarrow	<u>3</u>	<u>3</u>	2

Table 8. Diffusion inference time (in seconds/frame) comparison with previous diffusion-based video super-resolution tasks on $4\times$ upscaling 640×360 video.

Methods	UAVideo [2024]	MGLD [2024a]	Ours
Time (sec./frame)	31	54	67

score estimator. We use the RAFT [Teed and Deng 2020] model to estimate $OF(\cdot)$.

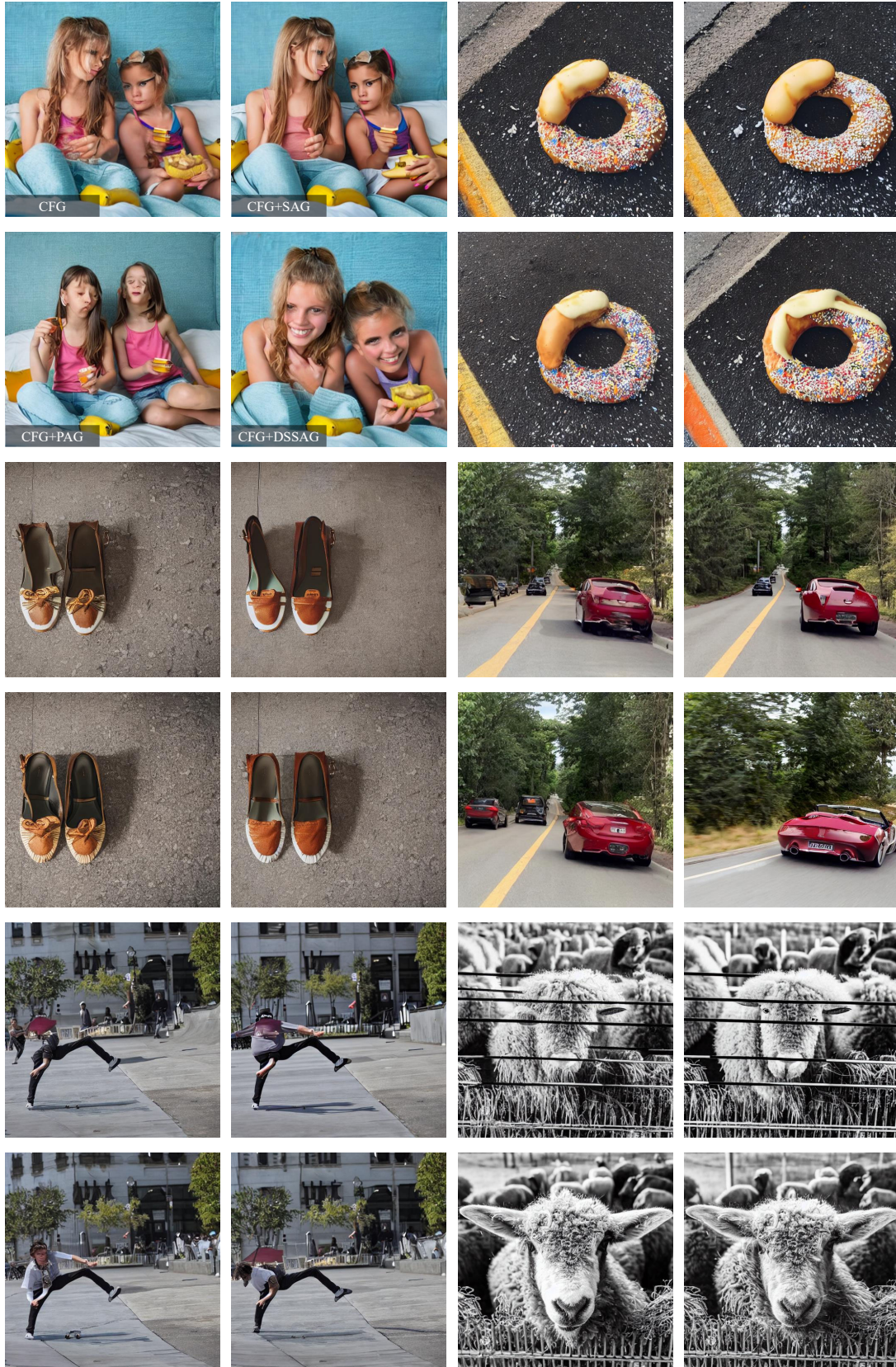


Fig. 13. Visualization of previous diffusion guidance approaches and our DSSAG. DSSAG combines well with CFG, while 1.5 \times faster than SAG [2023] and PAG [2024]. Images are generated using a diffusion model [CompVis 2022].